nanomaterials

MDPI

Article

Long-Term Exposure of MoS_2 to Oxygen and Water Promoted Armchair-to-Zigzag-Directional Line Unzippings

Youngho Song †, Minsuk Park †, Junmo Park, Hyun S. Ahn, Tae Kyu Kim and Sang-Yong Ju *

Department of Chemistry, Yonsei University, Seoul 03722, Korea; yh05song@yonsei.ac.kr (Y.S.); min4218@yonsei.ac.kr (M.P.); parkjunmo2000@yonsei.ac.kr (J.P.); ahnhs@yonsei.ac.kr (H.S.A.); tkkim@yonsei.ac.kr (T.K.K.)

* Correspondence: syju@yonsei.ac.kr

† These authors contributed equally to this work.

Abstract: Understanding the long-term stability of MoS_2 is important for various optoelectronic applications. Herein, we show that the long-term exposure to an oxygen atmosphere for up to a few months results in zigzag (zz)-directional line unzipping of the MoS_2 basal plane. In contrast to exposure to dry or humid N_2 atmospheres, dry O_2 treatment promotes the initial formation of line defects, mainly along the armchair (ac) direction, and humid O_2 treatment further promotes ac line unzipping near edges. Further incubation of MoS_2 for a few months in an O_2 atmosphere results in massive zz-directional line unzipping. The photoluminescence and the strain-doping plot based on two prominent bands in the Raman spectrum show that, in contrast to dry-N_2-treated MoS_2, the O_2-treated MoS_2 primarily exhibits hole doping, whereas humid-O_2-treated MoS_2 mainly exists in a neutral charge state with tension. This study provides a guideline for MoS_2 preservation and a further method for generating controlled defects.

Keywords: molybdenum disulfide; line defect; unzipping; zigzag; oxygen

Citation: Song, Y.; Park, M.; Park, J.; Ahn, H.S.; Kim, T.K.; Ju, S.-Y. Long-Term Exposure of MoS_2 to Oxygen and Water Promoted Armchair-to-Zigzag-Directional Line Unzippings. *Nanomaterials* **2022**, *12*, 1706. https://doi.org/10.3390/nano12101706

Academic Editor: Stefano Agnoli

Received: 2 May 2022
Accepted: 15 May 2022
Published: 17 May 2022

1. Introduction

Molybdenum disulfide (MoS_2) is a representative of the transition metal dichalcogenide (TMDC) MX_2 family which has sandwiched layer structures with the transition metal M (groups four, five, and six atoms) located between chalcogen atoms X (S, Se, and Te). Owing to the presence of a band gap associated with its few-atom-thick layers held together by van der Waals forces, MoS_2 possesses interesting optical [1–3], spin–valley polarization [4,5], and catalytic properties [6–8]. In the context of its optical properties, neutral MoS_2 displays two features known as A (~1.89 eV) and B (~2.08 eV) excitons [1,2,9], which are associated with direct transitions from the highest spin-split valence bands to the lowest conduction bands. Furthermore, the A exciton has subcomponents in the form of a charge-neutral exciton band A^o at 1.89 eV and a lower-lying charged exciton (trion) band A^- at 1.86 eV, whose relative intensities and positions are dependent on the doping [10–12] and strain (ε) [11,13–16] of MoS_2. Applications of the optoelectronic properties of MoS_2 require an understanding of its long-term stability.

MoS_2 is amenable to both electron (n) or hole (p) doping [10,11] and it can possess strain (ε) [11,13–16]. The effects of environmentally abundant oxygen and water on the optoelectronic properties of MoS_2 have been studied [17–19], but how these species affect the doping and ε properties of MoS_2 under ambient conditions remains largely unknown, and this is an important issue. Treatments under harsh oxidative conditions such as with oxygen plasma [18], UV-ozone [20], and high-temperature annealing (>300 °C) [18,21,22] are known to induce oxidation of the basal plane of MoS_2. Following these treatments, the basal plane of MoS_2 exhibits reduced photoluminescence (PL), while edges and cracked regions display increased PL, suggesting that oxidation plays different roles in governing the properties of the basal plane and periphery. Moreover, O_2 incubation of up to one year

leads to random cracks and defects [19]. In contrast, physisorption of oxygen by MoS_2 activated at 450 °C under vacuum results in a large basal-plane PL enhancement [17] caused by MoS_2-to-O_2 charge transfer. Because chemisorbed oxygen modulates the optical properties of MoS_2 differently from physisorbed oxygen, it is important to gain an understanding of how chemical oxidation controls the doping and ε, which in turn govern the band-gap structure of MoS_2 [12].

Theoretical study [23] suggests that the basal plane of MoS_2 exhibits a large kinetic barrier (i.e., 1.6 eV) for O_2 chemisorption, whereas vacancies (i.e., sulfur vacancies) at the surface of MoS_2 reduce the barrier to 0.8 eV. The experimentally determined activation energy for bulk MoS_2 oxidation (0.54 eV and 0.79 eV) [22,24] is somewhat lower than the theoretically predicted value. However, recent scanning tunneling microscope measurements [25] show that point-like oxygen-substitution reactions producing oxygenated MoS_2 occur spontaneously, even under ambient conditions. Along with the fact that Mo-terminated edges of MoS_2 readily react with O_2 [26], these findings indicate that oxygenated MoS_2 possesses various point defects which are randomly distributed over the plane.

The investigation described below was designed to address this issue. For this purpose, chemical vapor deposition (CVD)-grown MoS_2 crystals were exposed to four different conditions for two weeks: N_2, N_2 with 75% relative humidity (N_2-75RH), O_2, and O_2 with 75% relative humidity (O_2-75RH). Using various methods, including Raman spectroscopy, photoluminescence (PL) spectroscopy, and atomic force microscopy (AFM), we observed that the basal plane of MoS_2 possessing tensile strain (ε_T) associated with its preparation using CVD, undergoes zigzag (zz)-directional unzipping upon long-term exposure to an oxygen atmosphere. Specifically, during the initial phases of exposure to O_2 and O_2-75RH, MoS_2 crystals display initial macroscopic armchair (ac)-directional micrometer-scale defects near triangular edges. Following increased exposure times of up to a few months, the initial ac-directional defects near the periphery change into zz-directional unzipping in the basal plane. This unique unzipping behavior is associated with the susceptibility of S defects in the basal plane to tension caused by oxidation. Moreover, Raman and PL spectroscopic studies show that changes occurring in the optoelectronic properties of MoS_2 upon chemical oxidation are a consequence of changes in ε_T and doping.

2. Materials and Methods

2.1. Materials and Instrumentation

MoO_3 (product no. 267856, ACS reagents, purity $\geq$ 99.5%) and sulfur (product no. 13803, purity $\geq$ 99.5%) were purchased from Sigma-Aldrich (St. Louis, MO, USA). Sulfur was further recrystallized using vacuum sublimation at ca. 10^{-3} torr, as described previously [27]. Sodium cholate (SC), with a purity of over 98%, was purchased from TCI (Tokyo, Japan) and used as a surfactant and an adhesion promoter to a silicon substrate. Deionized water with a resistivity greater than 18 MΩ was used. All gases, including N_2, Ar, and O_2 with purities of over 99.99% were obtained from Donga Gas (Jinju, Korea). The 285-nm thick SiO_2/Si substrates (lot no. 7400397-601, Shin-Etsu, Tokyo, Japan) were spin-coated with MoO_3 and converted to MoS_2. The as-received wafer was cut into pieces of size 1.0 × 1.0 cm^2 and further rinsed with methanol, acetone, and isopropanol while undergoing bath sonication, then subjected to drying with a N_2 stream. Optical microscope (OM) images were obtained using an upright fluorescence microscope (BX-51, Olympus, Tokyo, Japan) with a CMOS camera (3.6 μm/pixel, 1280 × 1024 pixels, part no. DCC1645C, Thorlabs, Newton, NJ, USA) and a light-emitting diode light source (cold white color, part no. MCWHL2, Thorlabs) with an optional dichroic cube set (MWG, Olympus), which could image the 660 nm PL of MoS_2. SEM images were acquired using field-emission SEMs (SU8000, Hitachi or 7610f-plus, JEOL Ltd., Tokyo, Japan) operating at an acceleration voltage of 5 kV.

2.2. Precursor Preparation

MoS_2 growth involved the use of SC as adhesion promoter and surfactant for MoO_3 powder, according to the procedure described in the literature [28]. Aqueous MoO_3 dispersion was prepared by sonication using SC as a surfactant. Briefly, 20 mM MoO_3 was added to 1 wt. % SC in 100 mL of water. The suspension was subjected to bath sonication for 1 h (70 W, Branson1519, Brookfield, CT, USA) followed by tip sonication for 2 h (300 W amplitude, probe tip diameter: 13 mm, VCX 750, Sonics and Materials, Newtown, CT, USA). The dispersion was centrifuged using a table-top centrifuge (Wisespin CF-10, Daihan Scientific Co, Ltd., Wonju-si, Korea) to collect an 80% supernatant. 100 µL of the MoO_3 dispersion was spin-coated at 3000 rpm for 80 s by drop-casting on precleaned SiO_2 on a Si substrate. Sulfur was prepared by vacuum sublimation. Briefly, 1 g of sulfur was placed at the bottom of a sublimation kit with a cold finger. The sublimation temperature was set to 200 °C under vacuum (10^{-3} torr).

2.3. Growth of MoS_2 Crystal

MoS_2 was prepared by using a hot-wall CVD apparatus [29] operating at atmospheric pressure, with the aforementioned spin-coated MoO_3 and the sublimed sulfur powder as precursors, modified from the previous study [27]. Prior to the MoS_2 growth, a quartz tube in a tube furnace was pre-annealed for 30 min at 1000 °C with a 20 standard cubic centimeter per min (sccm) Ar flow to remove any physisorbed water, in a CVD chamber. After cooling, the MoO_3 spin-coated substrate was loaded into the hot zone of a tube furnace with the SiO_2 side face up, and an alumina boat containing 30 mg of sulfur was placed in an upstream position. Crystal growth was conducted at 750 °C for 20 min, at which time the alumina boat containing the sulfur reached ~220 °C. The substrate was then cooled to room temperature.

2.4. Environmental Control of MoS_2

Four different environments (i.e., N_2, N_2-75RH, O_2, and O_2-75RH) were prepared using a Schlenk line technique and a septum-capped vial, with precautions as follows. For the N_2-75RH or O_2-75RH environments, a vial containing saturated brine solution maintaining 75RH [30] was bubbled with the N_2 (or O_2) for 90 min using a syringe to remove any O_2 dissolved in the solution. For the N_2 or O_2 environments, a vial containing a moisture-absorbing silica gel was initially flame-dried thoroughly with a hand-held torch while a vacuum (10^{-3} torr) was pulled, and the sample was subsequently treated with a cycle of N_2 (or O_2) purging/vacuum, at least four times. Each sample was incubated for two weeks prior to any measurements. A further one month of incubation was conducted for observation of long-term changes.

2.5. Raman and PL Measurements

The samples were loaded into an environmental chamber (TS1000V-17/3 with T96-S, Linkam Scientific Instruments Ltd., Redhill, UK) which allowed observation of the sample through a coverslip while measurements were made. Raman and PL spectra were obtained using a micro-Raman spectroscopy setup with a backscattering geometry, as described in the literature [27,29,31]. Briefly, a spectrometer (Triax 320 with 1800 gr/mm) and coverslip-tolerant 40× objective (UPlanSApo, N.A.: 0.95, Olympus) were utilized to obtain the Raman and PL spectra. Calibration for Raman spectroscopy was conducted with multiple Hg/Ar lamp peaks using a light source (HG-1, Ocean Optics, Oxford, UK), according to the procedure described in the literature [29]. The Si peak at 520.89 cm^{-1} was used as an internal reference and an intensity-normalizing peak. Laser power was maintained below 0.06 mW to minimize any light-induced damage. The obtained Raman and PL spectra were further deconvoluted with Lorentzian fitting. Especially in the PL spectra, A°, A^{-}, and B excitons were fitted to an unrestricted position and area.

2.6. Construction of Coordination System for ε–n Plot

The Raman origin ((E^1_{2g}, A_{1g}) = (385.3 cm^{-1}, 404.8 cm^{-1})) for the ε and n plot was taken from the values derived from suspended MoS_2 in the literature [11]. Biaxial ε vs. n coordinates were introduced by modification of the ε–n diagram described previously [32–34], as in the case of graphene [35]. Since CVD-grown MoS_2 exhibits biaxial ε_T [36], biaxial ε_T and Raman responses were utilized [11]. The changes in in-plane vibration E^1_{2g} ($\Delta\omega_E$) and out-of-plane vibration A_{1g} ($\Delta\omega_A$) and their variations were $\Delta\omega_E = -5.2$ cm^{-1}/% and $\Delta\omega_A = -1.7$ cm^{-1}/%. Using the formula $\gamma = [\omega - \omega_0]/[2\varepsilon\omega_0]$, we determined the Grüneisen parameters γ for the Raman modes to be $\gamma_{E^1_{2g}} = 0.68$ and $\gamma_{A_{1g}} = 0.21$, with the slope per ε or $\Delta\omega_A/\Delta\omega_E = 0.35$ [11]. In the case of n, vibrational changes in E^1_{2g} and A_{1g} and their extents were $\Delta\omega_E = 0.21$ cm^{-1} and $\Delta\omega_A = 1.97$ cm^{-1} per 1×10^{12} cm^{-2}, with the slope of n with $\Delta\omega_A/\Delta\omega_E = 9.4$ [35].

2.7. AFM Measurements

AFM height and phase images were obtained by using a tapping mode with an NX-10 AFM (Park Systems, Suwon, Korea). Al-coated silicon cantilevers (force constant: 37 N/m, resonance frequency: 300 kHz, ACTA-20, App Nano, Mountain View, CA, USA) were used. Typically, 512 × 512 pixels for a 40 μm length were routinely acquired at a speed of 0.2 Hz. The XEI program (Park Systems, Korea) was used to flatten topographies along the fast axis of scan using a polynomial, by excluding speckles of size 5 nm.

3. Results

CVD-grown triangular MoS_2 crystals were single crystals terminated with zz edges [37] and were used to probe the effects of oxidation reactions on the morphological and optoelectronic properties. The MoS_2 crystals were grown by CVD, using the procedure developed in our previous investigation [27], starting with MoO_3 and sublimed sulfur (see Materials and Methods section). First, a well-dispersed aqueous MoO_3 dispersion containing 1 wt. % sodium cholate (SC) as a surfactant and adhesion promoter [28] was spin-coated onto a 285 nm thick SiO_2/Si substrate. After annealing at 1000 °C to eliminate adsorbates, a quartz tube was loaded with the MoO_3-coated substrate and a boat containing freshly sublimed sulfur. A 20 sccm Ar flow was used as a carrier gas and the temperature of the hot zone was raised to 750 °C for 20 min, to promote MoO_3 reduction with sulfur. The growth of the MoS_2 crystals was terminated by cooling the tube to room temperature for 40 min while maintaining the Ar flow.

The Initial characterization of the as-grown MoS_2 as a control was conducted using various methods, including optical microscopy (OM), atomic force microscopy (AFM), photoluminescence (PL) imaging/spectroscopy, and Raman spectroscopy (see Figure 1A–E). Inspection of the representative CVD-grown MoS_2 via the OM image (Figure 1A) shows the MoS_2 crystal as a ca. 46 μm long equilateral triangle with uniform contrast. The corresponding AFM height image (Figure 1B) shows that the crystal has a clean surface and a 0.70 nm edge height, indicating a monolayer of MoS_2 [37]. Notably, the PL image (Figure 1C) shows a gradient of PL brightening from the center to the peripheral regions. Other researchers [16,36] have found that such gradual PL intensity (I_{PL}) and peak position (λ) changes, as well as shifts in the Raman bands in CVD-grown MoS_2, occur when proceeding from the center to the peripheral regions owing to differences in tensile strain (ε_T) caused by thermal expansion coefficient differences between the Si substrate and the MoS_2. Since biaxial ε_T shifts the excitonic A band by −99 meV/% [11], the observed λ of 675 nm in the PL spectrum at the center (Figure 1D) suggests the presence of substantial ε_T (i.e., 0.4%) compared to that at peripheral regions where the λ is ca. 660 nm. The positions of the two characteristic Raman bands of the in-plane vibration E^1_{2g} and out-of-plane vibration A_{1g} are known to be sensitive to ε_T, and E^1_{2g} undergoes larger downfield shifts compared to A_{1g} with increasing ε_T [11,13–16,38]. The Raman spectrum of the central MoS_2 region (Figure 1E) contains E^1_{2g} at 383.1 cm^{-1} and A_{1g} at 406.2 cm^{-1} [39], whereas the spectra

at the peripheries contain upshifted 383.6 cm^{-1} and 406.8 cm^{-1} bands, which is in good agreement with reported spectra of MoS_2 under ε_T. The results suggest that ε_T is a major contributor to the anisotropy present in the PL and Raman spectra of the as-prepared MoS_2 crystal. Immediately after characterization, the MoS_2 crystals were incubated under the four different atmospheres N_2, N_2-75RH, O_2, and O_2-75RH for two weeks (see Figure S1A in the Supplementary Materials (SM) for schematics of the environmental incubation processes).

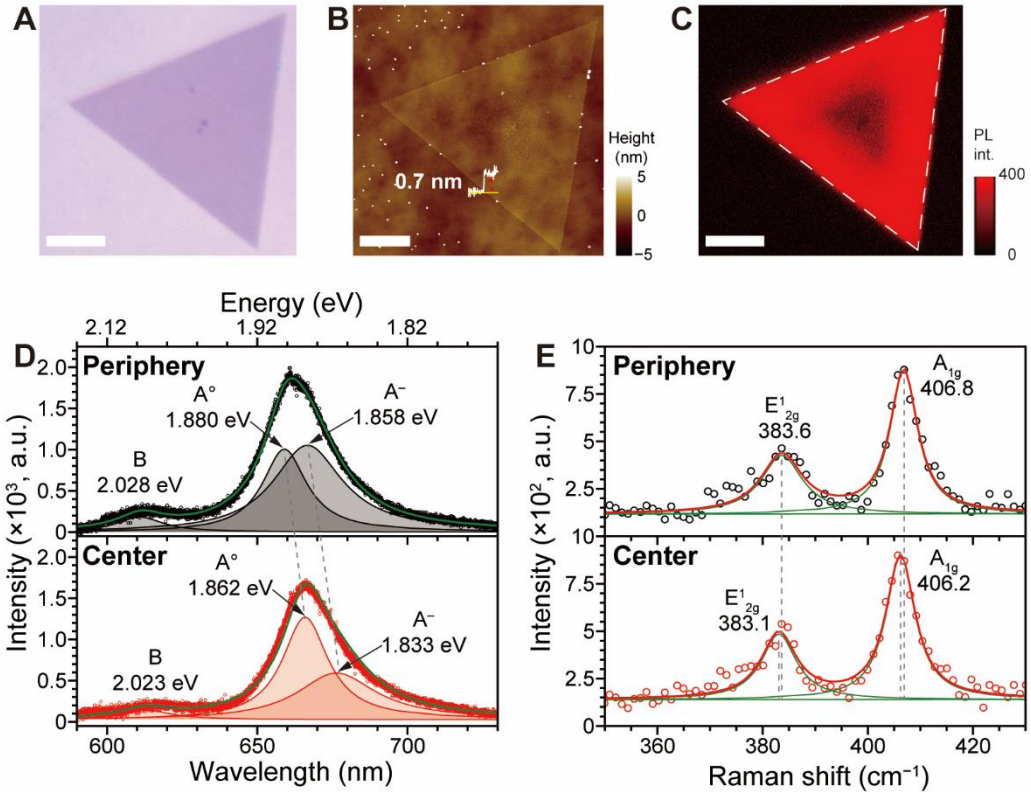

Figure 1. The characterizations of the as-grown MoS_2 grains by various methods: (**A**) OM image; (**B**) the corresponding AFM height topography; (**C**) PL image with emission filtered using a 660 nm bandpass filter. Scale bars: 10 µm. (**D**) PL spectra obtained from central and peripheral parts of MoS_2 and its Lorentzian deconvolutions to indicate A°, A^-, and B, respectively. Dashed lines are drawn for comparison of the position. (**E**) The corresponding Raman spectra (circles) and its Lorentzian deconvolutions (green).

The effects of various environments on the morphology of MoS_2 were first examined using AFM (Figure 2a–d). All crystals under the four conditions have triangular shapes and heights (white traces) varying from 0.6 to 0.85 nm, indicating monolayer MoS_2. While the N_2 and N_2-75RH samples (Figure 2a,b) have topographies similar to the as-grown material, surprisingly, the MoS_2 subjected to an O_2 atmosphere (Figure 2c) displays few micrometer-long directional line defects originating from the edges. These defects are more visible in the phase image (Figure S2C,D), compared to those from N_2-treated samples. Notably, the angles of the line defects against zz edges were ca. 30, 90, and 150° (see inset of Figure 2c), suggesting ac-directional line defects. This result contrasts with the report in [19] that aging of CVD-grown MoS_2 and WS_2 under ambient environmental conditions leads to random cracks and defects. This result suggests that the conditions for CVD growth affect the oxidative defects. Furthermore, the O_2-75RH-treated sample (Figure 2d) shows that unzipping occurs from the edges in the ac directions. The inset in Figure 2d shows that unzipping, instead of occurring at ac line defects, occurs at the edges, and that crack directions are at 120° from each other (see red arrows for the intersection). This result

suggests that dry and humid O_2 oxidations promote stepwise transformations in the MoS_2 crystal, from line defects to eventual unzipping.

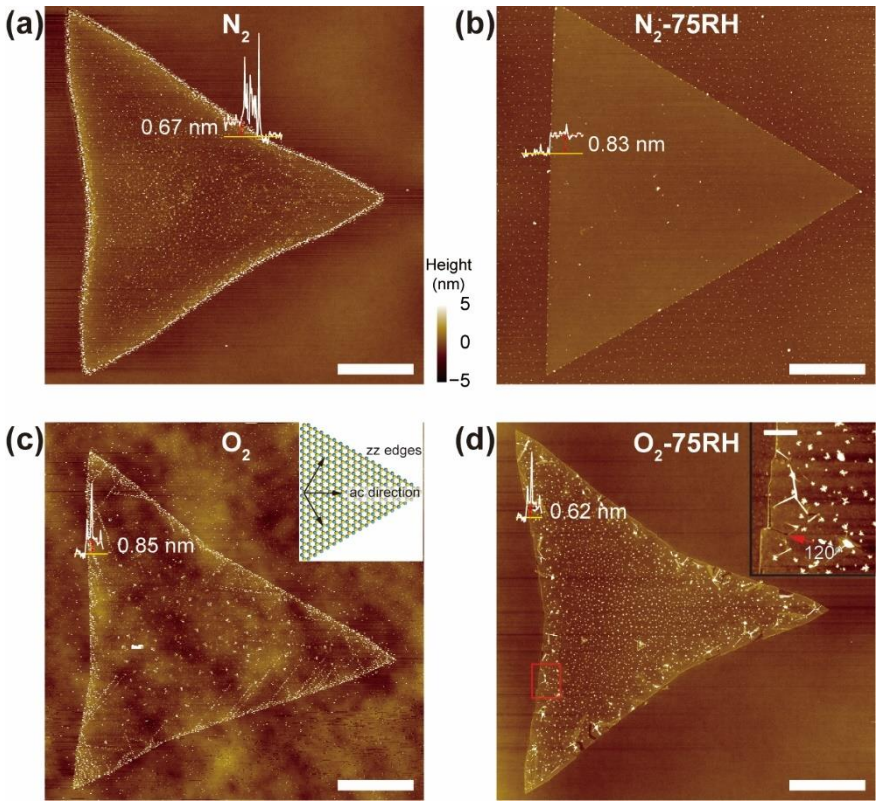

Figure 2. AFM height images of MoS_2 crystals treated with: (**a**) N_2; (**b**) N_2-75RH; (**c**) O_2; (**d**) O_2-75RH. White traces are height profiles of MoS_2. Inset of (**c**): crystallographic orientation of line defects of O_2-treated MoS_2, with Mo and S color-coded in green and yellow, respectively. Inset of (**d**): AFM height image of directional unzipping from MoS_2 edges in red box in (**d**). Scale bar: 10 μm for (**a**–**d**); 1 μm for the inset of (**d**).

Because unzipping typically begins at the mechanically weakest points, the line defects and the subsequent unzipping are likely to be correlated with the ε_T of the MoS_2, which in turn is associated with the optical properties of the MoS_2 crystal. Figure 3A–D show the corresponding PL images of the samples. The images show that the I_{PL} for the N_2-treated crystal gradually increases from the center to the periphery, suggesting that the ε_T behavior is similar to that of as-prepared MoS_2. Interestingly, the N_2-75RH sample (Figure 3B) has a uniform I_{PL} at both the center and periphery. A humid environment is known to form entrapped water between graphene and the substrate [40–42] or MoS_2 and the substrate [43]. To confirm that such entrapped water is related to the uniform I_{PL}, AFM height measurements of the basal plane from the N_2-75RH sample (Figure S3A) were made. Water was entrapped evenly over the sample, and water entrapped regions is 0.5 nm thick and a few micrometers wide (Figure S3B) were entrapped between the MoS_2 and the substrate. This was a phenomenon not seen in the N_2-treated sample. These results are in agreement with the previous study, which demonstrated that a monolayer of water adhered under the MoS_2 surface to a thickness of ~0.5 nm [43], as seen in other two-dimensional materials such as graphene [40–42]. This result suggests that the increased height induced by water and the subsequent strain might increase ε_T and lead to the observed uniform I_{PL} over the MoS_2 crystal.

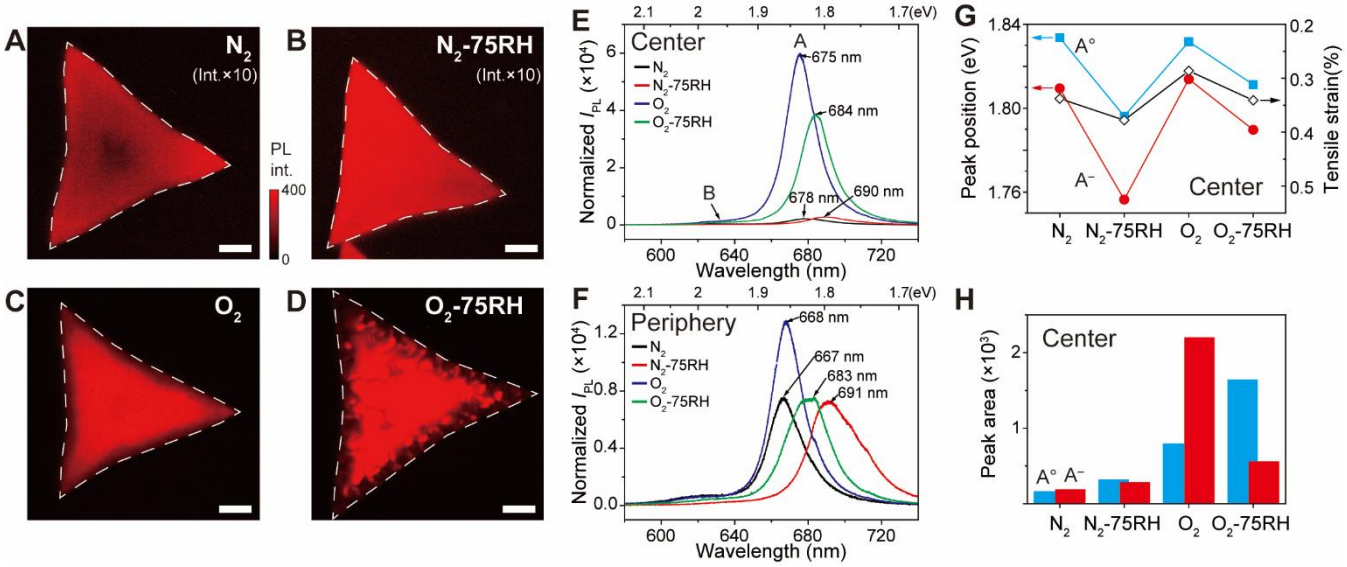

Figure 3. PL images, spectra, and analysis at central and peripheral positions of MoS_2 crystals after incubation for two weeks under each condition. PL images from: (**A**) N_2; (**B**) N_2-75RH; (**C**) O_2; (**D**) O_2-75RH samples. Scale bar: 10 μm. PL intensities of (**A**,**B**) were multiplied for visual comparison. Normalized PL spectra from (**E**) central, and (**F**) peripheral regions with respect to the 520.89 cm^{-1} Si peak. (**G**) PL peak position and (**H**) PL peak-area changes of A^o and A^- derived by each treatment from central regions.

The PL image from the O_2-treated sample (Figure 3C) shows that I_{PL} gradually increased from the periphery to the center, a trend that is opposite to that occurring in the N_2-treated sample. The low I_{PL} near the periphery overlaps with the AFM-observed line defects present in the O_2-treated MoS_2. These results suggest that, unlike for samples treated using harsh oxidations [18,20,22], physisorbed O_2 at the center of the crystal actually results in an enhancement of I_{PL}, which is in accordance with the previous report [17]. In contrast, chemically oxygenated species evidenced by line defects form near the periphery and result in the reduced I_{PL}. Similar to the O_2 sample, the crystal incubated under the O_2-75RH condition (Figure 3D) displays an I_{PL} that is brighter at the center and dimmer and more irregular at the periphery. Such spatial inhomogeneity originates from unzipping and folding of the MoS_2, as evidenced by comparing the PL and AFM images.

Qualitative information was gained about doping and ε_T by analyzing the PL spectra from the central (Figure 3E) and peripheral (Figure 3F) regions of the incubated MoS_2 crystals. Inspection of the spectra of the basal planes (Figure 3E) treated using humidified atmospheres (i.e., N_2-75RH and O_2-75RH) show that the λ values of the A bands display a bathochromic shift from 24 to 32 meV compared with those treated with N_2 and O_2 only. Moreover, the basal plane of the O_2-treated sample exhibits an I_{PL} about 11 times larger than that of the crystal exposed to N_2. The spectra from the peripheries (Figure 3F) show that while the peripheral I_{PL}s of the O_2 and O_2-75RH samples were lower than those associated with the basal plane, the peripheral I_{PL} of the N_2 sample was increased and that of N_2-75RH was unchanged. These results suggest that the center and periphery of the MoS_2 crystal experience different degrees of doping and ε_T.

The λ and I_{PL} of A^o and A^- peaks in the PL spectra of MoS_2 are dependent upon ε and n, and this serves as a foundation for deciphering the roles that O_2 and H_2O play in forming peripheral defects and unzipping [12,36]. To elucidate these values, the PL spectra at the central positions of the MoS_2 crystals were deconvoluted using Lorentzians (shaded area), as shown in Figure S4. As evidenced by the dashed lines, the λ values and peak areas of A^o and A^- underwent a systematic change for crystals treated using each condition. For example, among the four samples, the dry N_2- and O_2-treated samples exhibited the most blue-shifted λ values for the A^o and A^- peaks, suggesting that they are associated

with a smaller ε_T. In addition, the λ values of the A^o and A^- (Figure 3G) bands of samples treated using humid atmospheres exhibited proportional red shifts. A comparison of the relative areas of the A^o and A^- bands (Figure 3F), which provides information about the charge state of MoS_2 [10], shows that peak areas are much greater in the spectra of O_2 and O_2-75RH samples. Moreover, the comparison shows that water induces an increase in the population of the charge-neutral A^o state, and O_2 causes an increase in the area of the charged A^- state. This result is opposite to that of a previous study suggesting that water has a *p*-doping effect [43], and suggests that water promotes neutral exciton formation while physisorbed O_2 facilitates trion formation. Similar analysis of the PL spectra of peripheral regions (Figure S5A–C) shows that analogous but lesser shifts in λ occur (Figure S5B) and that the relative areas of A^o and A^- bands are relatively smaller compared to those in the spectra of basal planes. These observations in peripheral regions are in line with doping created by line defects and unzipping [19].

Raman spectroscopy is a powerful tool for gaining an understanding of the quantitative ε and *n*- or *p*-doping density of MoS_2, because these parameters are closely related to chemical bond strengthening or weakening, which alters the vibrational behavior. A previous study [35] showed that ε and *n* contributions in graphene are quantitatively associated with two Raman bands (i.e., G and 2D modes). A similar concept has been utilized to evaluate ε and *n* for monolayer MoS_2 [32–34]. To apply this treatment, we chose the frequencies from the spectra of suspended MoS_2 as an origin for the unperturbed, pristine state [44,45]. Utilizing the published values for ε and *n* of monolayer MoS_2 [11,46], an ε–*n* coordinate system in units of % and 1×10^{12} cm^{-2} (Figure 4c) was devised in a coordinate framework comprising two prominent Raman bands (E^1_{2g}, A_{1g}). Specifically, Figure 4c is a plot of ε (black dashed line) and *n* (red dashed line), with an origin O = (E^1_{2g}, A_{1g}) = (385.3, 404.8), corresponding to pristine MoS_2. In addition, ε_C values are compressive strains, and *n* and *p* denote *n* and *p* doping, respectively. Representative crystal spectra acquired from the center and periphery are shown in Figure 4a,b. It is noteworthy that Raman bands near 275 cm^{-1} corresponding to MoO_3 are not present [21]. As shown in Figure 4c, the central (peripheral) position of the N_2 sample displays two bands at 381.8 (383.1) and 403.8 (403.8) cm^{-1}. In terms of strain doping, the central part has ε–*n* coordinates of (0.34, −0.4), and the peripheral part has coordinates of (0.2, 0.7). This result suggests that while ε_T decreases from the center to the periphery, in accordance with previous findings [27,36], a slight *p*- to *n*-doping transition occurs simultaneously. The doping of the N_2-treated sample is likely to be related to the interaction of the basal MoS_2 with the SiO_2/Si substrate, which acts as a *p* dopant [29,35]. Compared to the N_2-treated sample, the N_2-75RH sample (orange) exhibited much higher ε_T values (from 0.37 to 0.42%) at both the central and peripheral positions and experienced only a negligible doping density change. This result further supports the idea of the presence of water-induced tensile strain. This result underscores the advantage of utilizing an ε–*n* plot for analyzing the spectroscopic data, because otherwise the *p*-doping and ε_T results are both included in a similar downshift in vibrational frequencies [11].

Inspection of the ε–*n* plot shows that the two prominent Raman bands (E^1_{2g} and A_{1g}) associated with the central and peripheral regions of the O_2- and N_2-treated MoS_2 crystals exhibited nearly similar movement along the *p*-doping axis. This observation suggests that O_2 treatment results in *p*-doping, which is in agreement with the occurrence of charge transfer from MoS_2 to physisorbed O_2 [17]. Finally, the O_2-75RH treated sample has ε–*n* coordinates of (0.4, −1) and (0.25, 1) for the central and peripheral positions, respectively. The different doping densities with different signs observed for the central and peripheral regions are closely connected to the existence of peripheral unzipping and folding, which decrease ε_T. The increase in ε_T and the charge neutralization taking place in changing from O_2 to O_2-75RH, in conjunction with the PL results, indicate that treatments with O_2 and H_2O lead predominantly to *p*-doping and ε_T, respectively.

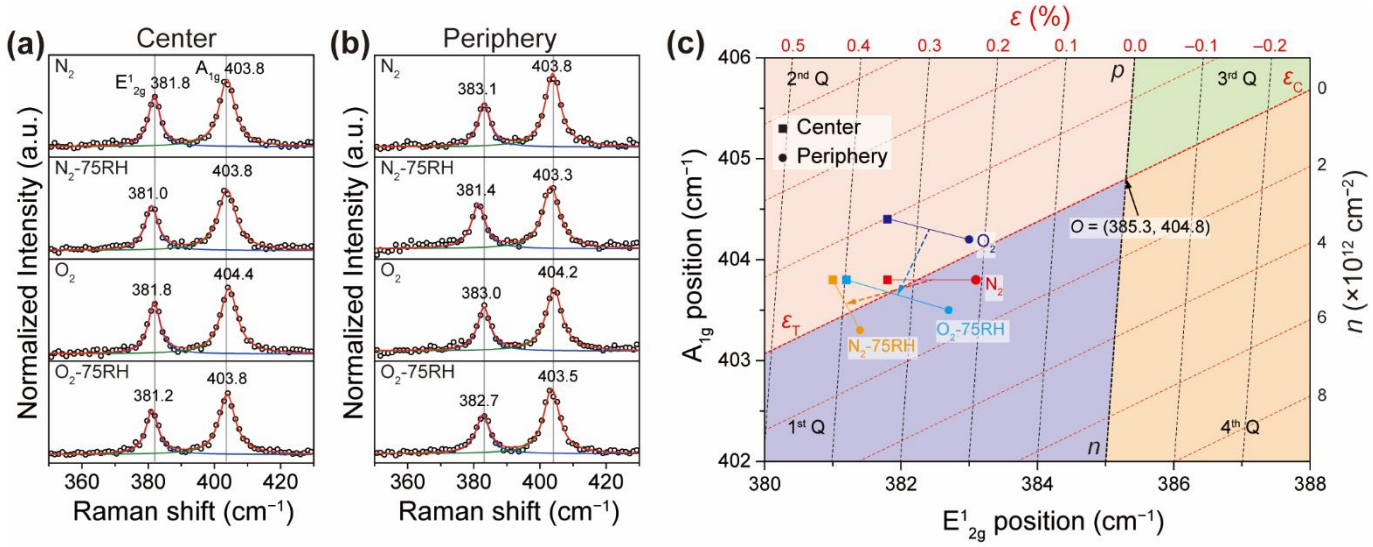

Figure 4. Raman spectra of (**a**) central and (**b**) peripheral regions from the incubated MoS_2 crystals. Excitation wavelength: 532 nm. Raman spectra were deconvoluted by Lorentzian shape analysis and normalized according to the Si peak at 520.84 cm^{-1} nm. (**c**) Plot of ε (black dashed line) and n (red dashed line) with origin O = (E^1_{2g}, A_{1g}) = (385.3, 404.8) extracted from Raman spectra of suspended MoS_2 sample. Here, ε_T and ε_C stand for tensile and compressive strains, respectively, and n and p denote n and p doping, respectively. Solid lines between Raman points are drawn for grouping the same samples.

The results suggest that regardless of the environmental conditions used, MoS_2 samples possess considerable ε_T, albeit with different doping densities. However, only O_2-treated crystals experienced line defects and unzipping. This observation prompted us to perform an experiment in which MoS_2 crystals were exposed to O_2 and O_2-75RH environments for three months. Figure 5A,D show the respective AFM phase images, facilitating the visualization of unzipping. Remarkably, both samples show zz-directional line unzipping with respect to zz-terminated edges. The O_2-treated sample had a wider unzipping width compared to the O_2-75RH-treated MoS_2. Unzippings occurred at 120° with respect to each other. Although unzipping near the periphery is ac-directional with respect to the edge, it changes to the zz direction in the basal plane. This finding stands in stark contrast to the etched triangular pit of exfoliated MoS_2 prepared by high-temperature annealing (i.e., 300 °C) [21,47] and the random cracks incubated at room temperature [19]. Inspection of the normalized PL spectra of the O_2-incubated crystal (Figure 5B) shows that both unzipping and basal positions occur at ~670 nm, which corresponds to the near-absence of tension. Similarly, both Raman spectra (Figure 5C) show similar interpeak separations (i.e., ~25 cm^{-1}). A similar unzipping behavior but associated with a larger difference in ε_T was observed for the O_2-75RH-treated sample. In this case, the PL peak position (Figure 5E) of the unzipped region (black circle in Figure 5D) displayed a large blue shift (20 nm) compared to that from the basal plane, showing that the ε_T was relieved. Raman spectra analysis (Figure 5F) further supported the fact that the basal plane has a larger ε_T (larger interpeak separation) compared to that for the O_2-treated crystal.

These defects are different from the defects that can exist in the as-grown state. Figure S6A,B show PL images of the as-prepared MoS_2 sample and the same sample after incubation. Bright PL originates from the crack or unzipping regions, showing an increase in line defects. However, the existing cracks in the as-prepared sample appear to be random, in contrast to the precise zz-directional unzipping after O_2-75RH treatment. The AFM phase image (Figure S6C) clearly shows that the O_2-75RH-treated sample had precise turns and angles of unzipping with respect to the edges. In addition, proceeding from the edges to the center slowly changed the unzipping direction from ac to zz lines. Figure S7 shows the AFM phase images from O_2- (Figure S7A–C) and O_2-75RH-treated

(Figure S7D–F) samples. Irrespective of the presence of H_2O, nearly all the ac unzipping at the edges changed into the zz direction in the basal plane within a few micrometers. Interestingly, the width of the ac unzipping is much less than that of the zz unzipping, presumably owing to the ε_T difference in the central and peripheral regions. Along with the PL and Raman studies, this finding strongly supports the fact that directional unzipping is dependent on ε.

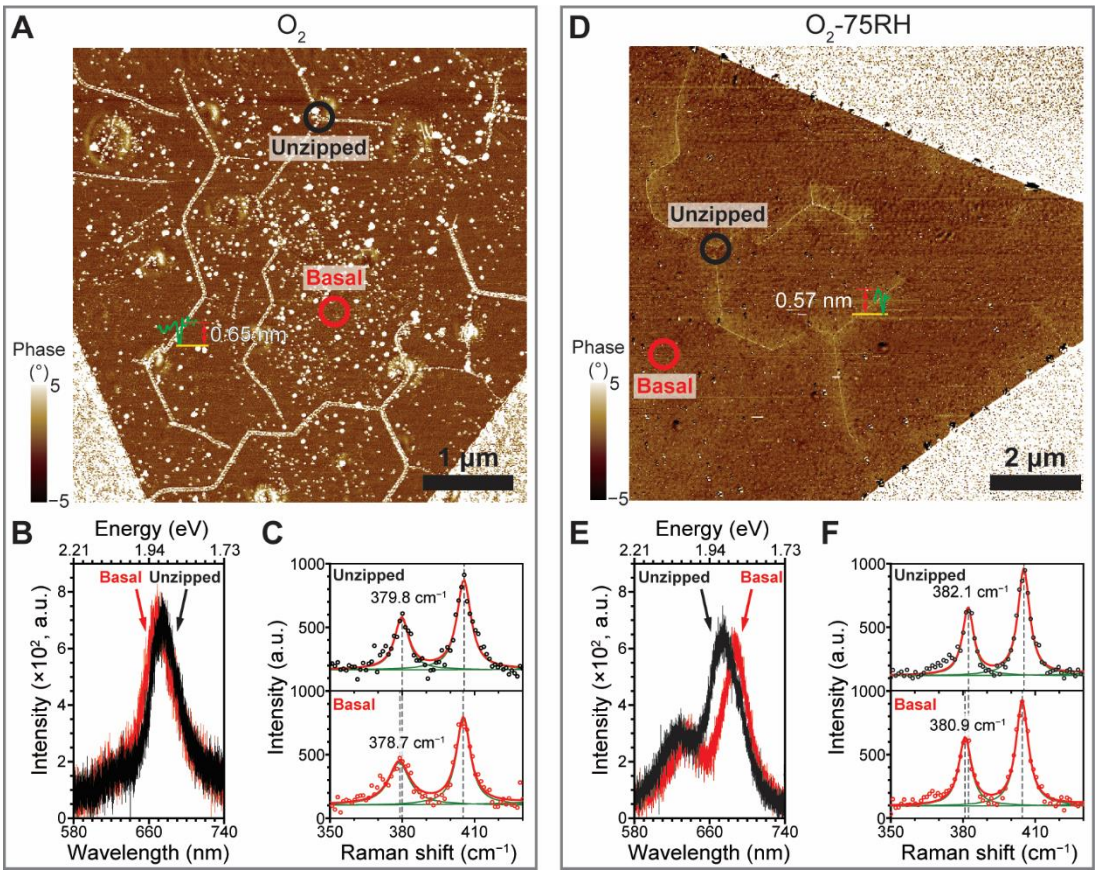

Figure 5. The zz-directional line unzipping of MoS_2 induced by a three-month exposure to O_2 and O_2-75RH environments. (**A**) AFM phase image of MoS_2 with O_2. (**B**) Corresponding normalized PL spectra and (**C**) Raman spectra obtained from marked positions in (**A**). Line profile was obtained from the corresponding height image. Raman bands were deconvoluted by Lorentzian shape analysis. (**D**) AFM phase image of MoS_2 after three-month incubations with O_2-75RH. (**E**) Corresponding PL spectra and (**F**) Raman spectra obtained from marked positions in (**D**).

The AFM image (Figure 6A) reveals details of the zz-directional line unzipping and origin. The O_2-treated sample shows 45 nm wide unzipping. The width is persistent along the unzipped segments. In addition, the 120° turns are very sharp. Since the observed typical ε_T is in the range of 0.2–0.4%, the width of the MoS_2 grain extends by 20–40 nm, which accounts for the few unzippings with a 45 nm width. Similarly, the AFM phase image of the O_2-75RH sample (Figure 6B), which has similar ε_T, displays somewhat similar line width (i.e., 30 nm). As evidenced by Figure S7, typical unzipping occurs in two or three lines along the 10 μm wide MoS_2 crystals, in good agreement with the observed line unzipping. Moreover, MoS_2 with a few layers also has similar unzipping. Figure S7A–C shows the AFM and corresponding OM images of MoS_2 with a few layers. The few-layered regions have less line unzipping compared to single-layered MoS_2. In addition, line unzipping is much more random, as indicated by the yellow arrows. We speculate that this effect of fewer and more random unzippings originates from the lesser ε_T exerted on few-layered MoS_2.

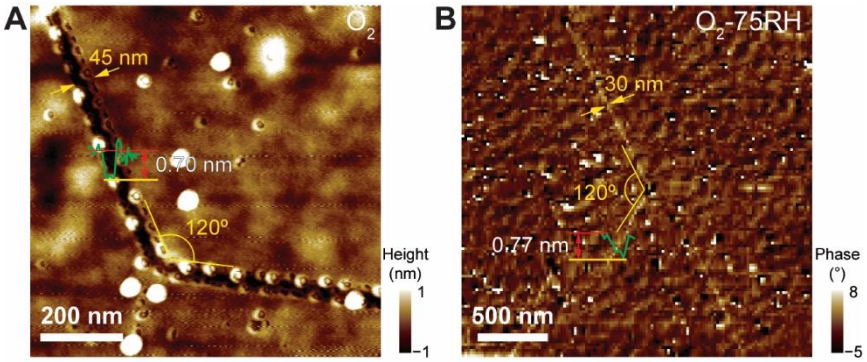

Figure 6. (**A**) AFM height image of line unzipping from O_2-treated MoS_2 sample. (**B**) AFM phase image of line unzipping from O_2-75RH-treated MoS_2 sample. It is noteworthy that the phase image was selected to display cracks. Line profile was obtained from the corresponding height image.

The remaining question to be addressed is that of how O_2 treatment causes MoS_2 to unzip along the zz directions. Raman spectroscopic analysis did not show the presence of detectable signals associated with MoO_3. In addition, the energy dispersive spectrum (EDS) using scanning electron microscopy (SEM) was also used to attempt to probe the nature of line defects, and this only showed strong Si and O signals from the substrate (Figure S8A–C). Mo-terminated edges readily produce oxygenated Mo. Because the Mo–O bond length (ca. 2.1 Å) [23] is shorter than that (ca. 2.4 Å) of Mo–S, additional ε_T should exist near the substitution defect sites, facilitating initial unzipping. Proceeding to zz unzipping seems to be associated with abundant S vacancies in CVD-grown MoS_2 [48], which are expected to be much higher than the S vacancies present in exfoliated MoS_2 (i.e., ranging from 5×10^{12} to 5×10^{13} cm^{-2}) [49]. The S vacancies accumulate and are transformed into O-substituted defects with high density up to 1×10^{15} cm^{-2} upon long-term exposure to ambient conditions [25]. Furthermore, the transmission electron microscopy study [50] showed that, at a high e-beam dose, S vacancies are formed owing to the excision of S atoms. Then, ac line defects up to a few tens of nanometers form as a result of the accumulation of S vacancies by adjacent S diffusion in the MoS_2 sheet before forming a zz unzipping. Therefore, the formation and accumulation of S vacancies represent a possible model for the formation of directional unzipping near the center. Directional unzipping change from ac to zz is likely to be associated with a larger ε_T in the basal plane than at the peripheries.

4. Conclusions

In summary, in the study described above, we found that initial armchair-directional line defects and subsequent zigzag-directional line unzipping occurred upon treatment with O_2. Moreover, we showed that these phenomena originate from tension in the chemical-vapor-deposition-grown monolayer MoS_2 crystals, caused by the thermal expansion coefficient difference with the substrate. The O_2-treated MoS_2 crystal exhibited armchair-directional line defects, and the inclusion of water in the incubation atmosphere resulted in further unzipping and folding of MoS_2. Raman and photoluminescence spectroscopic studies revealed that different prevailing tensions exist in MoS_2 grown by CVD under the four different conditions. Oxygenated defects, along with tension, further facilitated zigzag line unzipping in the MoS_2 basal plane upon long-term exposure to an O_2 atmosphere. The observations provide a potential strategy for directionally selective engineering of the MoS_2 basal plane as part of efforts to prepare novel building blocks such as MoS_2 nanoribbons [51]. In addition, the analysis developed for assessing the net contributions of O_2 and H_2O utilizing a strain-doping plot should be useful for the understanding of redox and catalytic effects.

Supplementary Materials: The following supporting information can be downloaded at: https://www.mdpi.com/article/10.3390/nano12101706/s1. Figure S1: Schematics of environmental incubations for MoS_2-containing substrates; Figure S2: AFM phase images of the sample; Figure S3: AFM height images of entrapped water; Figure S4: A° and A^{-} contributions to PL spectra from central regions of MoS_2; Figure S5: PL spectrum analysis of the peripheral regions of MoS_2 treated by different environments; Figure S6: PL image and AFM phase image of MoS_2 before and after O_2-75RH treatment for three months; Figure S7: The ac-to-zz directional unzipping change, proceeding from edges to center; Figure S8: EDS of selected area from zz unzipped samples.

Author Contributions: Conceptualization, writing, and supervision: S.-Y.J.; methodology: Y.S., M.P., and J.P.; funding acquisition: T.K.K., S.-Y.J. and H.S.A., All authors have read and agreed to the published version of the manuscript.

Funding: This research was funded by the Basic Science Research Program through the National Research Foundation of Korea (NRF) funded by the Ministry of Education, Science, and Technology (NRF-2022R1A2C1006932, NRF-2020R1F1A1076983 and NRF-2020R1A4A1017737).

Data Availability Statement: Not applicable.

Conflicts of Interest: The authors declare no conflict of interest.

References

1. Splendiani, A.; Sun, L.; Zhang, Y.; Li, T.; Kim, J.; Chim, C.-Y.; Galli, G.; Wang, F. Emerging Photoluminescence in Monolayer MoS_2. *Nano Lett.* **2010**, *10*, 1271–1275. [CrossRef] [PubMed]
2. Mak, K.F.; Lee, C.; Hone, J.; Shan, J.; Heinz, T.F. Atomically Thin MoS_2: A New Direct-Gap Semiconductor. *Phys. Rev. Lett.* **2010**, *105*, 136805. [CrossRef]
3. Shi, H.; Yan, R.; Bertolazzi, S.; Brivio, J.; Gao, B.; Kis, A.; Jena, D.; Xing, H.G.; Huang, L. Exciton Dynamics in Suspended Monolayer and Few-Layer MoS_2 2D Crystals. *ACS Nano* **2013**, *7*, 1072–1080. [CrossRef]
4. Xiao, D.; Liu, G.-B.; Feng, W.; Xu, X.; Yao, W. Coupled Spin and Valley Physics in Monolayers of MoS_2 and Other Group-VI Dichalcogenides. *Phys. Rev. Lett.* **2012**, *108*, 196802. [CrossRef] [PubMed]
5. Mak, K.F.; He, K.; Shan, J.; Heinz, T.F. Control of Valley Polarization in Monolayer MoS_2 by Optical Helicity. *Nat. Nanotechnol.* **2012**, *7*, 494–498. [CrossRef] [PubMed]
6. Hinnemann, B.; Moses, P.G.; Bonde, J.; Jørgensen, K.P.; Nielsen, J.H.; Horch, S.; Chorkendorff, I.; Nørskov, J.K. Biomimetic Hydrogen Evolution: MoS_2 Nanoparticles as Catalyst for Hydrogen Evolution. *J. Am. Chem. Soc.* **2005**, *127*, 5308–5309. [CrossRef]
7. Jaramillo, T.F.; Jørgensen, K.P.; Bonde, J.; Nielsen, J.H.; Horch, S.; Chorkendorff, I. Identification of Active Edge Sites for Electrochemical H_2 Evolution from MoS_2 Nanocatalysts. *Science* **2007**, *317*, 100–102. [CrossRef]
8. Li, Y.; Wang, H.; Xie, L.; Liang, Y.; Hong, G.; Dai, H. MoS_2 Nanoparticles Grown on Graphene: An Advanced Catalyst for the Hydrogen Evolution Reaction. *J. Am. Chem. Soc.* **2011**, *133*, 7296–7299. [CrossRef]
9. Evans, B.L.; Young, P.A.; Ditchburn, R.W. Optical absorption and dispersion in molybdenum disulphide. *Proc. R. Soc. Lond. A* **1965**, *284*, 402–422. [CrossRef]
10. Mak, K.F.; He, K.; Lee, C.; Lee, G.H.; Hone, J.; Heinz, T.F.; Shan, J. Tightly Bound Trions in Monolayer MoS_2. *Nat. Mater.* **2013**, *12*, 207–211. [CrossRef]
11. Lloyd, D.; Liu, X.; Christopher, J.W.; Cantley, L.; Wadehra, A.; Kim, B.L.; Goldberg, B.B.; Swan, A.K.; Bunch, J.S. Band Gap Engineering with Ultralarge Biaxial Strains in Suspended Monolayer MoS_2. *Nano Lett.* **2016**, *16*, 5836–5841. [CrossRef] [PubMed]
12. Mouri, S.; Miyauchi, Y.; Matsuda, K. Tunable Photoluminescence of Monolayer MoS_2 via Chemical Doping. *Nano Lett.* **2013**, *13*, 5944–5948. [CrossRef] [PubMed]
13. Castellanos-Gomez, A.; Roldán, R.; Cappelluti, E.; Buscema, M.; Guinea, F.; van der Zant, H.S.J.; Steele, G.A. Local Strain Engineering in Atomically Thin MoS_2. *Nano Lett.* **2013**, *13*, 5361–5366. [CrossRef] [PubMed]
14. Zhang, C.; Li, M.-Y.; Tersoff, J.; Han, Y.; Su, Y.; Li, L.-J.; Muller, D.A.; Shih, C.-K. Strain Distributions and Their Influence on Electronic Structures of WSe_2–MoS_2 Laterally Strained Heterojunctions. *Nat. Nanotechnol.* **2018**, *13*, 152–158. [CrossRef]
15. Island, J.O.; Kuc, A.; Diependaal, E.H.; Bratschitsch, R.; van der Zant, H.S.J.; Heine, T.; Castellanos-Gomez, A. Precise and Reversible Band Gap Tuning in Single-Layer $MoSe_2$ by Uniaxial Strain. *Nanoscale* **2016**, *8*, 2589–2593. [CrossRef]
16. McCreary, A.; Ghosh, R.; Amani, M.; Wang, J.; Duerloo, K.-A.N.; Sharma, A.; Jarvis, K.; Reed, E.J.; Dongare, A.M.; Banerjee, S.K.; et al. Effects of Uniaxial and Biaxial Strain on Few-Layered Terrace Structures of MoS_2 Grown by Vapor Transport. *ACS Nano* **2016**, *10*, 3186–3197. [CrossRef]
17. Tongay, S.; Zhou, J.; Ataca, C.; Liu, J.; Kang, J.S.; Matthews, T.S.; You, L.; Li, J.; Grossman, J.C.; Wu, J. Broad-Range Modulation of Light Emission in Two-Dimensional Semiconductors by Molecular Physisorption Gating. *Nano Lett.* **2013**, *13*, 2831–2836. [CrossRef]
18. Nan, H.; Wang, Z.; Wang, W.; Liang, Z.; Lu, Y.; Chen, Q.; He, D.; Tan, P.; Miao, F.; Wang, X.; et al. Strong Photoluminescence Enhancement of MoS_2 through Defect Engineering and Oxygen Bonding. *ACS Nano* **2014**, *8*, 5738–5745. [CrossRef]

19. Gao, J.; Li, B.; Tan, J.; Chow, P.; Lu, T.-M.; Koratkar, N. Aging of Transition Metal Dichalcogenide Monolayers. *ACS Nano* **2016**, *10*, 2628–2635. [CrossRef]
20. Jung, C.; Yang, H.I.; Choi, W. Effect of Ultraviolet-Ozone Treatment on MoS_2 Monolayers: Comparison of Chemical-Vapor-Deposited Polycrystalline Thin Films and Mechanically Exfoliated Single Crystal Flakes. *Nanoscale Res. Lett.* **2019**, *14*, 278. [CrossRef]
21. Yamamoto, M.; Einstein, T.L.; Fuhrer, M.S.; Cullen, W.G. Anisotropic Etching of Atomically Thin MoS_2. *J. Phys. Chem. C* **2013**, *117*, 25643–25649. [CrossRef]
22. Grønborg, S.S.; Thorarinsdottir, K.; Kyhl, L.; Rodriguez-Fernández, J.; Sanders, C.E.; Bianchi, M.; Hofmann, P.; Miwa, J.A.; Ulstrup, S.; Lauritsen, J.V. Basal Plane Oxygen Exchange of Epitaxial MoS_2 without Edge Oxidation. *2D Mater.* **2019**, *6*, 045013. [CrossRef]
23. Kc, S.; Longo, R.C.; Wallace, R.M.; Cho, K. Surface Oxidation Energetics and Kinetics on MoS_2 Monolayer. *J. Appl. Phys.* **2015**, *117*, 135301. [CrossRef]
24. Rao, R.; Islam, A.E.; Campbell, P.M.; Vogel, E.M.; Maruyama, B. In situ Thermal Oxidation Kinetics in Few Layer MoS_2. *2D Mater.* **2017**, *4*, 025058. [CrossRef]
25. Pető, J.; Ollár, T.; Vancsó, P.; Popov, Z.I.; Magda, G.Z.; Dobrik, G.; Hwang, C.; Sorokin, P.B.; Tapasztó, L. Spontaneous Doping of the Basal Plane of MoS_2 Single Layers through Oxygen Substitution under Ambient Conditions. *Nat. Chem.* **2018**, *10*, 1246–1251. [CrossRef]
26. Longo, R.C.; Addou, R.; Kc, S.; Noh, J.-Y.; Smyth, C.M.; Barrera, D.; Zhang, C.; Hsu, J.W.P.; Wallace, R.M.; Cho, K. Intrinsic Air Stability Mechanisms of Two-Dimensional Transition Metal Dichalcogenide Surfaces: Basal versus Edge Oxidation. *2D Mater.* **2017**, *4*, 025050. [CrossRef]
27. Koo, E.; Lee, Y.; Song, Y.; Park, M.; Ju, S.-Y. Growth Order-Dependent Strain Variations of Lateral Transition Metal Dichalcogenide Heterostructures. *ACS. Appl. Electron. Mater.* **2019**, *1*, 113–121. [CrossRef]
28. Han, G.H.; Kybert, N.J.; Naylor, C.H.; Lee, B.S.; Ping, J.; Park, J.H.; Kang, J.; Lee, S.Y.; Lee, Y.H.; Agarwal, R.; et al. Seeded Growth of Highly Crystalline Molybdenum Disulphide Monolayers at Controlled Locations. *Nat. Commun.* **2015**, *6*, 6128. [CrossRef]
29. Koo, E.; Ju, S.-Y. Role of Residual Polymer on Chemical Vapor Grown Graphene by Raman Spectroscopy. *Carbon* **2015**, *86*, 318–324. [CrossRef]
30. Brien, F.E.M.O. The Control of Humidity by Saturated Salt Solutions. *J. Sci. Instrum.* **1948**, *25*, 73. [CrossRef]
31. Koo, E.; Kim, S.; Ju, S.-Y. Relationships between the Optical and Raman Behavior of Van Hove Singularity in Twisted Bi- and Fewlayer Graphenes and Environmental Effects. *Carbon* **2017**, *111*, 238–247. [CrossRef]
32. Chaste, J.; Missaoui, A.; Huang, S.; Henck, H.; Ben Aziza, Z.; Ferlazzo, L.; Naylor, C.; Balan, A.; Johnson, A.T.C.; Braive, R.; et al. Intrinsic Properties of Suspended MoS_2 on SiO_2/Si Pillar Arrays for Nanomechanics and Optics. *ACS Nano* **2018**, *12*, 3235–3242. [CrossRef] [PubMed]
33. Rao, R.; Islam, A.E.; Singh, S.; Berry, R.; Kawakami, R.K.; Maruyama, B.; Katoch, J. Spectroscopic Evaluation of Charge-Transfer Doping and Strain in Graphene/MoS_2 Heterostructures. *Phys. Rev. B* **2019**, *99*, 195401. [CrossRef]
34. Michail, A.; Delikoukos, N.; Parthenios, J.; Galiotis, C.; Papagelis, K. Optical Detection of Strain and Doping Inhomogeneities in Single Layer MoS_2. *Appl. Phys. Lett.* **2016**, *108*, 173102. [CrossRef]
35. Lee, J.E.; Ahn, G.; Shim, J.; Lee, Y.S.; Ryu, S. Optical Separation of Mechanical Strain from Charge Doping in Graphene. *Nat. Commun.* **2012**, *3*, 1024. [CrossRef] [PubMed]
36. Liu, Z.; Amani, M.; Najmaei, S.; Xu, Q.; Zou, X.; Zhou, W.; Yu, T.; Qiu, C.; Birdwell, A.G.; Crowne, F.J.; et al. Strain and Structure Heterogeneity in MoS_2 Atomic Layers grown by Chemical Vapour Deposition. *Nat. Commun.* **2014**, *5*, 5246. [CrossRef]
37. van der Zande, A.M.; Huang, P.Y.; Chenet, D.A.; Berkelbach, T.C.; You, Y.; Lee, G.-H.; Heinz, T.F.; Reichman, D.R.; Muller, D.A.; Hone, J.C. Grains and Grain Boundaries in Highly Crystalline Monolayer Molybdenum Disulphide. *Nat. Mater.* **2013**, *12*, 554–561. [CrossRef]
38. Frisenda, R.; Drüppel, M.; Schmidt, R.; Michaelis de Vasconcellos, S.; Perez de Lara, D.; Bratschitsch, R.; Rohlfing, M.; Castellanos-Gomez, A. Biaxial Strain Tuning of the Optical Properties of Single-Layer Transition Metal Dichalcogenides. *Npj 2D Mater. Appl.* **2017**, *1*, 10. [CrossRef]
39. Lee, C.; Yan, H.; Brus, L.E.; Heinz, T.F.; Hone, J.; Ryu, S. Anomalous Lattice Vibrations of Single- and Few-Layer MoS_2. *ACS Nano* **2010**, *4*, 2695–2700. [CrossRef]
40. Xu, K.; Cao, P.; Heath, J.R. Graphene Visualizes the First Water Adlayers on Mica at Ambient Conditions. *Science* **2010**, *329*, 1188–1191. [CrossRef]
41. Lee, D.; Ahn, G.; Ryu, S. Two-Dimensional Water Diffusion at a Graphene–Silica Interface. *J. Am. Chem. Soc.* **2014**, *136*, 6634–6642. [CrossRef] [PubMed]
42. Ma, M.; Tocci, G.; Michaelides, A.; Aeppli, G. Fast Diffusion of Water Nanodroplets on Graphene. *Nat. Mater.* **2016**, *15*, 66–71. [CrossRef]
43. Varghese, J.O.; Agbo, P.; Sutherland, A.M.; Brar, V.W.; Rossman, G.R.; Gray, H.B.; Heath, J.R. The Influence of Water on the Optical Properties of Single-Layer Molybdenum Disulfide. *Adv. Mater.* **2015**, *27*, 2734–2740. [CrossRef]
44. Lee, J.-U.; Kim, K.; Cheong, H. Resonant Raman and Photoluminescence Spectra of Suspended Molybdenum Disulfide. *2D Mater.* **2017**, *2*, 044003. [CrossRef]

45. Yan, R.; Simpson, J.R.; Bertolazzi, S.; Brivio, J.; Watson, M.; Wu, X.; Kis, A.; Luo, T.; Hight Walker, A.R.; Xing, H.G. Thermal Conductivity of Monolayer Molybdenum Disulfide Obtained from Temperature-Dependent Raman Spectroscopy. *ACS Nano* **2014**, *8*, 986–993. [CrossRef]
46. Chakraborty, B.; Bera, A.; Muthu, D.V.S.; Bhowmick, S.; Waghmare, U.V.; Sood, A.K. Symmetry-Dependent Phonon Renormalization in Monolayer MoS_2 Transistor. *Phys. Rev. B* **2012**, *85*, 161403. [CrossRef]
47. Zhou, H.; Yu, F.; Liu, Y.; Zou, X.; Cong, C.; Qiu, C.; Yu, T.; Yan, Z.; Shen, X.; Sun, L.; et al. Thickness-Dependent Patterning of MoS_2 Sheets with Well-Oriented Triangular Pits by Heating in Air. *Nano Res.* **2013**, *6*, 703–711. [CrossRef]
48. Hong, J.; Hu, Z.; Probert, M.; Li, K.; Lv, D.; Yang, X.; Gu, L.; Mao, N.; Feng, Q.; Xie, L.; et al. Exploring Atomic Defects in Molybdenum Disulphide Monolayers. *Nat. Commun.* **2015**, *6*, 6293. [CrossRef]
49. Vancsó, P.; Magda, G.Z.; Pető, J.; Noh, J.-Y.; Kim, Y.-S.; Hwang, C.; Biró, L.P.; Tapasztó, L. The Intrinsic Defect Structure of Exfoliated MoS_2 Single Layers Revealed by Scanning Tunneling Microscopy. *Sci. Rep.* **2016**, *6*, 29726. [CrossRef]
50. Ryu, G.H.; Lee, J.; Kim, N.Y.; Lee, Y.; Kim, Y.; Kim, M.J.; Lee, C.; Lee, Z. Line-Defect Mediated Formation of Hole and Mo Clusters in Monolayer Molybdenum Disulfide. *2D Mater.* **2016**, *3*, 014002. [CrossRef]
51. Reiss, P.; Protière, M.; Li, L. Core/Shell Semiconductor Nanocrystals. *Small* **2009**, *5*, 154–168. [CrossRef] [PubMed]